

Light curves and polarization of accretion- and nuclear-powered millisecond pulsars

K. Viironen and J. Poutanen

Astronomy Division, Department of Physical Sciences, P.O. Box 3000, FIN-90014 University of Oulu, Finland
e-mail: kerttu.viironen@oulu.fi, juri.poutanen@oulu.fi

November 9, 2018

Abstract. We study theoretical X-ray light curves and polarization properties of accretion-powered millisecond pulsars. We assume that the radiation is produced in two antipodal spots at the neutron star surface which are associated with the magnetic poles. We compute the angle-dependent intensity and polarization produced in an electron-scattering dominated plane-parallel accretion shock in the frame of the shock. The observed flux, polarization degree and polarization angle are calculated accounting for special and general relativistic effects. The calculations also extended to the case of nuclear-powered millisecond pulsars – X-ray bursts. In this case, we consider one spot and the radiation is assumed to be produced in the atmosphere of the infinite Thomson optical depth. The light curves and polarization profiles show a large diversity depending on the model parameters. Presented results can be used as a first step to understand the observed pulse profiles of accretion- and nuclear-powered millisecond pulsars. Future observations of the X-ray polarization will provide a valuable tool to test the geometry of the emission region and its physical characteristics.

Key words. methods: numerical – polarization – pulsars: individual (SAX J1808.4–3658, XTE J1751–305) – stars: neutron – stars: oscillations – X-rays: binaries

1. Introduction

Since the discovery of pulsars in the 1960s, determination of the equation of state of neutron stars based on measuring their mass-radius relation was one of the main research goals. Radio pulsars have been used extensively for the mass determination (Thorsett & Chakrabarty 1999), but hardly can help to get any constraints on the neutron star radius since the radio emission is probably produced far from the surface. Observations of the isolated neutron stars emitting thermal radiation from their surface on the other hand is much more suited for the radius determination using the Stefan-Boltzmann law. Some of the radii determined this way from the X-ray emission (e.g. Drake et al. 2002; Thoma et al. 2004) are much smaller than any of the equation of state allow, pointing either to the existence of the more compact strange stars or (more likely) to a surface temperature gradient.

Statistical studies of the pulse profiles from standard X-ray pulsars also have been used to put constraints on the geometry of the emission region as well as the star compactness (Bulik et al. 2003). The problem here is that the accretion rate is close to the (local) Eddington, the magnetic field strongly affects the radiative transport resulting in rather complicated pulse profiles at low energies, and therefore it is difficult to predict from the first principles the angular distribution of the radiation escaping the emission region.

Quasi-periodic oscillations (QPO) observed in a number of low-mass X-ray binaries (van der Klis 2000), if produced in the inner part of the accretion disk, could be used to put weak constraints on the neutron star mass as well as its radius (see e.g. Miller et al. 1998). However, this method is indirect. Discovery of millisecond coherent pulsations during X-ray bursts in 13 low-mass X-ray binaries (so called nuclear-powered millisecond pulsars, see reviews by Strohmayer 2001; Strohmayer & Bildsten 2003) and in the persistent emission of five sources (accretion-powered millisecond pulsars, see review by Wijnands 2004) opens a completely new range of possibilities. The emission in these cases is produced at the surface of a rapidly spinning neutron star and the observed pulse profiles and oscillation amplitudes are strongly affected by special as well as general relativistic effects (Braje et al. 2000; Weinberg et al. 2001; Poutanen & Gierliński 2003, hereafter PG03). Weak magnetic field in these sources does not affect the radiative transport and thus a much more reliable prediction for the radiation pattern from the surface can be obtained. This tightens the possible range of other parameters. However, similar light curves still can be produced with a very different set of parameters. For example, exchanging inclination with the magnetic inclination (angle between magnetic and rotational axis) has almost no effect on the light curve.

A possible way to distinguish between the models is to observe the behaviour of the polarization degree and polarization angle with phase. Polarization has proven to be a valuable tool

Send offprint requests to: J. Poutanen

in determining the geometry of the emission region in radio pulsars (e.g. Blaskiewicz et al. 1991). Polarimetric observations in the X-ray range could also be possible in the near future (see Costa et al. 2001; Bellazzini et al. 2003; Marshall et al. 2003). In this paper, we perform theoretical calculations of the light curves and polarization behaviour in accretion- and nuclear-powered millisecond pulsars accounting for relativistic effects. The presented models could be used to determine the physical parameters of the X-ray millisecond pulsars.

2. Method

We assume that the emission originates in one or two antipodal (in the case of accreting ms pulsars) spots at the neutron star surface. The hard X-rays are produced by thermal Comptonization in a plane-parallel slab (accretion shock) of optical depth of order unity (PG03). The emission during the X-ray bursts is assumed to be produced in a semi-infinite electron scattering dominated atmosphere. The radiation pattern is assumed to have azimuthal symmetry in the comoving frame of a spot. We compute the Stokes parameters in this frame and transform them to the observer frame. First, we make the Lorentz transformation to the non-rotating frame accounting for Doppler boosting and relativistic aberration and then follow photon trajectories to the observer at infinity in Schwarzschild space-time. Deviations from the Schwarzschild metric due to the stellar rotation have a small effect (Braje et al. 2000) and are neglected here. For pulsar rotational frequencies of $\nu \gtrsim 400$ Hz, we also need to account for time delays which in the extreme cases can reach about 5–10 per cent of the pulsar period.

Lorentz transformation and gravitational light bending do not change the polarization degree and the observed value can be found if one knows the polar angle at which a photon is emitted in the spot comoving frame. For a slowly rotating star, the polarization vector lies in the plane formed by the spot normal (spot radius-vector) and the line of sight as in the rotating vector model of Radhakrishnan & Cooke (1969). This vector rotates if a star is rapidly spinning (Ferguson 1973, 1976).

In the following calculations we assume two identical antipodal point-like spots, of which both, or only one is visible depending on the parameters. We follow the method described in detail in PG03 for the flux computations and extend it to the description of the polarization degree and polarization angle.

2.1. General definitions

Let S' be a surface element (spot) at colatitude θ (see Fig. 1 for the geometry). (Quantities with primes correspond to the frame comoving with the spot.) The second spot is situated at the opposite side of the star. Let i be the inclination of the spin axis and the unit vector in the direction to the observer $\mathbf{k} = (\sin i, 0, \cos i)$ lies in the (x, z) plane. The coordinates of the spots vary periodically and the unit vector of the spot normal is $\mathbf{n} = \pm(\sin \theta \cos \phi, \sin \theta \sin \phi, \cos \theta)$, where the upper sign corresponds to the spot closer to the observer (primary) and the lower sign to the antipodal spot (secondary). Thus the angle

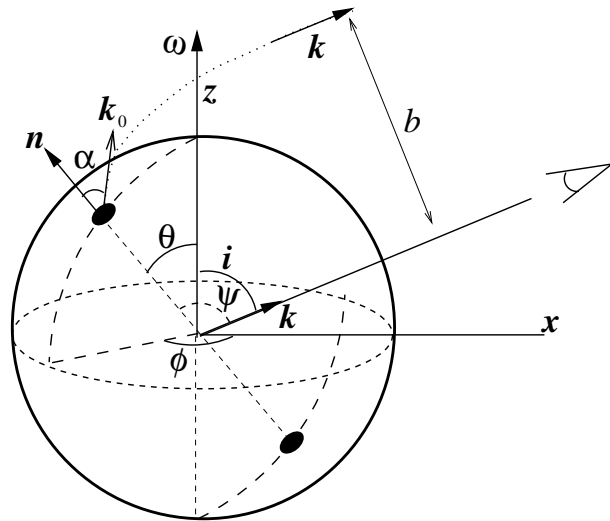


Fig. 1. Geometry of the problem.

between the direction to the spot and the line of sight is given by

$$\cos \psi \equiv \mathbf{k} \cdot \mathbf{n} = \pm(\cos i \cos \theta + \sin i \sin \theta \cos \phi), \quad (1)$$

where the pulsar rotational phase ϕ is zero when the primary spot is closest to the observer.

In Schwarzschild metric the photon orbits are planar and the original direction of the photon \mathbf{k}_0 near the stellar surface is then (PG03):

$$\mathbf{k}_0 = [\sin \alpha \mathbf{k} + \sin(\psi - \alpha) \mathbf{n}] / \sin \psi, \quad (2)$$

where α is the angle between \mathbf{k}_0 and \mathbf{n} , i.e. $\cos \alpha = \mathbf{k}_0 \cdot \mathbf{n}$.

The intensity of radiation and its polarization at a given pulsar phase ϕ depend on the angle α' between an emitted photon and the local normal to the stellar surface in the spot comoving frame

$$\cos \alpha' = \delta \cos \alpha, \quad (3)$$

where δ is the Doppler factor. It can be expressed as

$$\delta = 1/[\gamma(1 - \beta \cos \xi)], \quad (4)$$

where $\gamma = (1 - \beta^2)^{-1/2}$ and β is the spot velocity in units of speed of light as measured in the non-rotating frame:

$$\beta = \frac{2\pi R}{c} \frac{v}{\sqrt{1 - r_g/R}} \sin \theta. \quad (5)$$

Here the observed pulsar frequency ν is corrected for the redshift $\sqrt{1 - r_g/R}$, where $r_g \equiv 2GM/c^2$ is the Schwarzschild radius of the star of mass M and radius R . The angle ξ between the spot velocity $\boldsymbol{\beta}/\beta = (\mp \sin \phi, \pm \cos \phi, 0)$ and \mathbf{k}_0 can be obtained from Eq. (2):

$$\cos \xi \equiv \frac{\boldsymbol{\beta}}{\beta} \cdot \mathbf{k}_0 = \frac{\sin \alpha \boldsymbol{\beta}}{\sin \psi \beta} \cdot \mathbf{k} = \mp \frac{\sin \alpha}{\sin \psi} \sin i \sin \phi. \quad (6)$$

2.2. Light bending and time delay

Due to the gravitational bending of light the angle at which the radiation is observed is different from the actual emission angle (see Fig. 1). The relation between angles α and ψ can be obtained by computing an elliptical integral (Pechenick et al. 1983):

$$\psi = \int_R^\infty \frac{dr}{r^2} \left[\frac{1}{b^2} - \frac{1}{r^2} \left(1 - \frac{r_g}{r} \right) \right]^{-1/2}, \quad (7)$$

where the impact parameter

$$b = \frac{R}{\sqrt{1 - r_g/R}} \sin \alpha. \quad (8)$$

For many purposes one can use a simpler expression derived by Beloborodov (2002, hereafter B02):

$$\cos \alpha \approx \cos \psi \left(1 - \frac{r_g}{R} \right) + \frac{r_g}{R}, \quad (9)$$

which gives an accuracy of the order of a few percent for $R \gtrsim 2.5r_g$. The spot is visible when $\cos \alpha > 0$. In Beloborodov's approximation this corresponds to $\cos \psi > -r_g/(R - r_g)$.

The difference in light travel time around the star becomes larger for more compact stars. A photon of impact parameter b is lagging one with the impact parameter 0 by (Pechenick et al. 1983):

$$c\Delta t(b) = \int_R^\infty \frac{dr}{1 - r_g/r} \left\{ \left[1 - \frac{b^2}{r^2} \left(1 - \frac{r_g}{r} \right) \right]^{-1/2} - 1 \right\}. \quad (10)$$

For rough estimations one can use an approximation $\Delta t(b) \approx R(1 - \cos \psi)/c$. If we compute the phase delays relative to photons emitted at $\phi = 0$, then the observed phase is approximately

$$\phi_{\text{obs}} \approx \phi + \Delta\phi_0(1 - \cos \phi), \quad (11)$$

where

$$\Delta\phi_0 = \cos i \cos \theta 2\pi\nu R/c. \quad (12)$$

For small delays, this expression can be reversed to

$$\begin{aligned} \cos \phi &\approx \cos \phi_{\text{obs}} + \Delta\phi_0 \sin \phi_{\text{obs}}(1 - \cos \phi_{\text{obs}}), \\ \sin \phi &\approx \sin \phi_{\text{obs}} + \Delta\phi_0 \cos \phi_{\text{obs}}(1 - \cos \phi_{\text{obs}}). \end{aligned} \quad (13)$$

2.3. Observed intensity and flux

The combined effect of the gravitational redshift and Doppler effect results in the following relation between the monochromatic observed and local intensities (see e.g. Misner et al. 1973; Rybicki & Lightman 1979):

$$I_E = \left(\frac{E}{E'} \right)^3 I_{E'}(\alpha') \quad (14)$$

where $E/E' = \delta \sqrt{1 - r_g/R}$. Here $I_{E'}(\alpha')$ is the intensity computed in the frame comoving with the spot. For the bolometric intensity, one gets

$$I = \left(\delta \sqrt{1 - r_g/R} \right)^4 I'(\alpha'). \quad (15)$$

If the radiation spectrum can be represented by a power-law $I_{E'}(\alpha') \propto E'^{-(\Gamma-1)}$ (as in accretion-powered ms pulsars) with the photon spectral index Γ which does not depend on the angle α' , then

$$I'_{E'}(\alpha') = I'_E(\alpha') \left(\delta \sqrt{1 - r_g/R} \right)^{\Gamma-1}. \quad (16)$$

This approximation is equivalent to the assumption of a weak energy dependence of the angular distribution. In the case of thermal Comptonization, it can be used if the maximum Doppler shift $\Delta\delta \sim 2\pi\nu R/c \sin i \sin \theta$ is smaller than the typical (relative) energy separation between photons of subsequent scattering orders $\Delta E/E \sim 4kT_e/m_e c^2$, where T_e is the electron temperature. This condition is equivalent to $(\nu/600 \text{ Hz}) \sin i \sin \theta < kT_e/16 \text{ keV}$, which is always satisfied in accreting pulsars. Then, the observed photons at a given energy E belong mostly to a certain scattering order ($n = 0, 1, 2, \dots$) which can be determined from

$$\frac{E}{E_0} = \left(1 + \frac{4kT_e}{m_e c^2} \right)^n, \quad (17)$$

where E_0 is the mean energy (at infinity) of the seed photon black body distribution.

In order to compute the observed flux, we need to know variations of the solid angle occupied by the spot on the observer's sky (PG03):

$$\Omega = \frac{S' \cos \alpha'}{D^2} \frac{1}{1 - r_g/R} \frac{d \cos \alpha}{d \cos \psi}. \quad (18)$$

where D is the source distance. (This transforms to $\Omega \approx S' \cos \alpha'/D^2$ in Beloborodov's approximation, since $d \cos \alpha/d \cos \psi \approx 1 - r_g/R$.) Hence the monochromatic flux becomes:

$$F_E = I_E \Omega = (1 - r_g/R)^{1/2} \delta^4 I'_{E'}(\alpha') \cos \alpha \frac{d \cos \alpha}{d \cos \psi} \frac{S'}{D^2}, \quad (19)$$

where we used aberration formula (3). The bolometric flux is given by:

$$F = (1 - r_g/R) \delta^5 I'(\alpha') \cos \alpha \frac{d \cos \alpha}{d \cos \psi} \frac{S'}{D^2}. \quad (20)$$

For a power-law spectrum, the monochromatic flux is

$$F_E = (1 - r_g/R)^{(\Gamma+2)/2} \delta^{\Gamma+3} I'_{E'}(\alpha') \cos \alpha \frac{d \cos \alpha}{d \cos \psi} \frac{S'}{D^2}. \quad (21)$$

In the following calculations we have used Eqs. (20) and (21) (with $\Gamma = 2$) for the black body and power-law spectra, respectively. We normalize the fluxes with $F_0 = 2(1 - r_g/R)^2 \frac{S'}{D^2} \int_0^1 \mu I'(\mu) d\mu$.

2.4. Polarization degree and polarization angle

Relativistic effects do not change the polarization degree and thus we take it equal to the polarization in the spot comoving frame $P'_{E'}(\alpha')$. However, when calculating the polarization degree of the total flux from both spots, the difference in the tilt of the polarization ellipses (difference caused by the time delay and different relativistic rotations) need to be considered.

In order to describe polarization, we introduce the main polarization basis,

$$\mathbf{e}_1^m = \frac{\hat{\omega} - \cos i \mathbf{k}}{\sin i}, \quad \mathbf{e}_2^m = \frac{\mathbf{k} \times \hat{\omega}}{\sin i}, \quad (22)$$

where $\hat{\omega}$ denotes the unit vector along the stellar rotational axis. In the absence of relativistic rotation of the polarization plane (for a slowly rotating star), the polarization vector lies in the plane formed by the local normal \mathbf{n} and the direction to the observer \mathbf{k} . The corresponding polarization basis is

$$\mathbf{e}_1 = \frac{\mathbf{n} - \cos \psi \mathbf{k}}{\sin \psi}, \quad \mathbf{e}_2 = \frac{\mathbf{k} \times \mathbf{n}}{\sin \psi}. \quad (23)$$

The polarization angle (PA) χ_0 measured from the projection of the spin axis on the plane of the sky in the counter-clockwise direction is given by:

$$\begin{aligned} \cos \chi_0 &= \mathbf{e}_1^m \cdot \mathbf{e}_1 = \mathbf{e}_2^m \cdot \mathbf{e}_2 = \frac{\sin i \cos \theta - \cos i \sin \theta \cos \phi}{\sin \psi}, \\ \sin \chi_0 &= \mathbf{e}_2^m \cdot \mathbf{e}_1 = -\mathbf{e}_1^m \cdot \mathbf{e}_2 = -\frac{\sin \theta \sin \phi}{\sin \psi}. \end{aligned} \quad (24)$$

We thus get

$$\tan \chi_0 = -\frac{\sin \theta \sin \phi}{\sin i \cos \theta - \cos i \sin \theta \cos \phi}. \quad (25)$$

This expression neglects the rotation of the polarization plane due to relativistic motion (e.g. Ferguson 1973, 1976). To correct for that we introduce the polarization basis related to the photon direction close to the neutron star surface \mathbf{k}_0 :

$$\mathbf{e}_1^0 = \frac{\mathbf{n} - \cos \alpha \mathbf{k}_0}{\sin \alpha}, \quad \mathbf{e}_2^0 = \frac{\mathbf{k}_0 \times \mathbf{n}}{\sin \alpha} = \mathbf{e}_2. \quad (26)$$

The equality $\mathbf{e}_2^0 = \mathbf{e}_2$ is related to the fact that photon trajectories are planar. If the polarization vector in the spot rest frame lies in the meridional plane, then it will be transformed to (Nagirner & Poutanen 1993)

$$\mathbf{e}'_1 = \frac{\mathbf{n} + \delta \gamma \cos \alpha (\boldsymbol{\beta} - \mathbf{k}_0)}{\sqrt{1 - \delta^2 \cos^2 \alpha}} \quad (27)$$

in the non-rotating frame. Thus, the rotation of the polarization vector due to relativistic motion is given by

$$\cos \chi_c = \mathbf{e}'_1 \cdot \mathbf{e}_1^0, \quad \sin \chi_c = \mathbf{e}'_1 \cdot \mathbf{e}_2^0, \quad (28)$$

which is reduced to (Poutanen, in preparation)

$$\tan \chi_c = \beta \cos \alpha \frac{\cos i \sin \theta - \sin i \cos \theta \cos \phi}{\sin \alpha \sin \psi + \beta \sin i \sin \phi}. \quad (29)$$

This correction angle depends linearly on the spot velocity β and, therefore, is negligible for spin frequencies $\nu \lesssim 300$ Hz. Since the angle χ_c is constant for parallel transport along the photon trajectory, the total polarization angle for each spot is

$$\chi = \chi_0 + \chi_c. \quad (30)$$

When we plot polarization angles for individual spots, we rotate it by $\pi/2$ (in any direction) if the polarization $P = Q/I$ is negative (i.e. dominant electric vector oscillations are perpendicular to the meridional plane defined by the spot normal and the direction of photon propagation).

For each spot calculations provide us with the Stokes vector $(F_I, F_Q, 0)^T$ (we do not consider sources of circular polarization), where flux F_I is computed using Eqs. (20) or (21), $F_Q = PF_I$, and the polarization degree P at angle α' is computed for a given optical depth of the slab (see below Eqs. (39) and (41)). We rotate this vector to the main basis

$$\begin{pmatrix} 1 & 0 & 0 \\ 0 & \cos 2\chi & -\sin 2\chi \\ 0 & \sin 2\chi & \cos 2\chi \end{pmatrix} \begin{pmatrix} F_I \\ F_Q \\ 0 \end{pmatrix} = \begin{pmatrix} F_I \\ F_Q \cos 2\chi \\ F_Q \sin 2\chi \end{pmatrix}. \quad (31)$$

Denoting the corresponding quantities for the primary and secondary spots by indices p and s, respectively, we get for the total observed Stokes vector

$$\begin{pmatrix} F_I^p + F_I^s \\ F_Q^p \cos 2\chi_p + F_Q^s \cos 2\chi_s \\ F_Q^p \sin 2\chi_p + F_Q^s \sin 2\chi_s \end{pmatrix}. \quad (32)$$

The degree of polarization is then obviously

$$P = \frac{\sqrt{(F_Q^p)^2 + (F_Q^s)^2 + 2F_Q^p F_Q^s \cos(2\chi_p - 2\chi_s)}}{F_I^p + F_I^s}, \quad (33)$$

and the total polarization angle is given by

$$\tan 2\chi_{\text{tot}} = \frac{F_Q^p \sin 2\chi_p + F_Q^s \sin 2\chi_s}{F_Q^p \cos 2\chi_p + F_Q^s \cos 2\chi_s}. \quad (34)$$

3. Local intensity and polarization

3.1. Radiative transfer in the accretion shock

We assume that the accretion shock can be represented as a plane-parallel slab which horizontal size is much larger than its vertical height so that the photons escaping from the sides of the slab can be ignored. This is a good approximation for moderate luminosities (Basko & Sunyaev 1976) typical for accretion-powered millisecond pulsars (Wijnands 2004). We calculate the angle-dependent intensity and the polarization degree of radiation emerging from the emission region, assuming Thomson scattering and corresponding polarization. The calculations are carried out following the procedure described in Sunyaev & Titarchuk (1985). Unpolarized seed soft photons are assumed to be injected from the neutron star surface (i.e. bottom of the slab). The boundary conditions are

$$I_{l,r}(\tau = 0, \mu) = I_{l,r}(\tau = \tau_0, -\mu) = 0, \quad 0 \leq \mu \equiv \cos \theta \leq 1, \quad (35)$$

where θ is the angle between photon direction and the outward slab normal, indices l, r refer to the polarizations in the meridional plane and perpendicular to it, respectively. The Thomson optical depth τ is measured from the bottom of the slab. The intensity of unscattered photons is given by:

$$I_{l,r}^0(\tau, \mu) = I_0 e^{-\tau/\mu}. \quad (36)$$

The intensity of n times scattered photons can be computed from

$$I_l^n(\tau, \mu) = \int_0^\tau \exp\left(-\frac{\tau - \tau'}{\mu}\right)$$

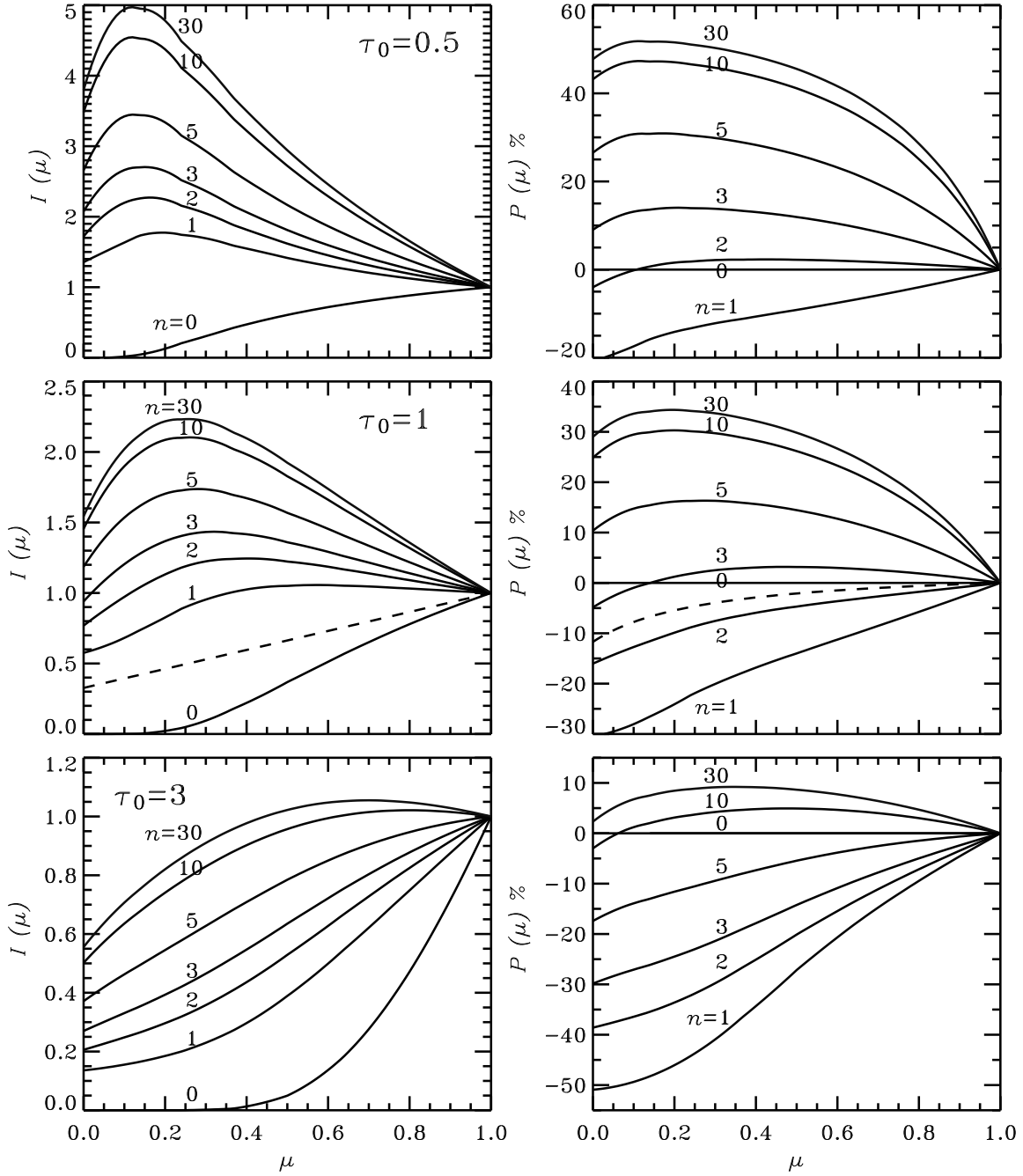


Fig. 2. Intensity (normalized to unity at $\mu = 1$) and polarization of the radiation escaping from a slab of Thomson optical depth $\tau_0 = 0.5, 1, 3$ for different scattering orders n . The unpolarized seed photons with intensity $I(\mu) = 1$ are injected from the bottom of the slab. The dashed curves show the intensity and polarization corresponding to the classical results of Chandrasekhar-Sobolev for the semi-infinite atmosphere $\tau_0 = \infty$.

$$\begin{aligned}
 & \times \left\{ (1 - \mu^2)A^n(\tau') + \mu^2 [B^n(\tau') + C^n(\tau')] \right\} \frac{d\tau'}{\mu}, \\
 I_r^n(\tau, \mu) &= \int_0^\tau \exp\left(-\frac{\tau - \tau'}{\mu}\right) [B^n(\tau') + C^n(\tau')] \frac{d\tau'}{\mu}, \quad (37) \\
 B^n(\tau) &= \frac{3}{8} \int_0^1 \mu'^2 [I_l^{n-1}(\tau, \mu') + I_r^{n-1}(\tau, -\mu')] d\mu', \quad (38) \\
 C^n(\tau) &= \frac{3}{8} \int_0^1 [I_r^{n-1}(\tau, \mu') + I_l^{n-1}(\tau, -\mu')] d\mu'.
 \end{aligned}$$

where the quantities $A^n(\tau)$, $B^n(\tau)$ and $C^n(\tau)$ are as follows

$$A^n(\tau) = \frac{3}{4} \int_0^1 (1 - \mu'^2) [I_l^{n-1}(\tau, \mu') + I_l^{n-1}(\tau, -\mu')] d\mu',$$

The intensities $I_{l,r}^n(\tau, -\mu)$ can be computed in a similar way by changing the integration boundaries in Eqs. (37) from $(0, \tau)$ to (τ, τ_0) . These equations are similar to those in Sunyaev & Titarchuk (1985), but we do not assume symmetrical (relative to the slab central plane) distribution of seed photons. Finally,

the degree of polarization of the radiation leaving the slab upper boundary is

$$P = Q(\tau_0, \mu) / I(\tau_0, \mu), \quad (39)$$

where the Stokes parameters are

$$\begin{aligned} I(\tau_0, \mu) &= I_l(\tau_0, \mu) + I_r(\tau_0, \mu), \\ Q(\tau_0, \mu) &= I_l(\tau_0, \mu) - I_r(\tau_0, \mu). \end{aligned} \quad (40)$$

The results of calculations for different scattering orders are presented in Fig. 2.

Due to the symmetry, the polarization vector can be either in the meridional plane (positive polarization) or perpendicular to it (negative polarization). The polarization degree is zero for the seed radiation ($n = 0$), negative for small scattering orders and for $\tau_0 = 1$ becomes positive at $n \gtrsim 3$. The polarization degree also depends on the electron temperature. At high electron temperatures, the electron random motions produce different aberrations and in the electron rest frame photons are scattered at different angles. This reduces the polarization degree (Poutanen 1994; Poutanen & Svensson 1996). Thus, for example, for $kT_e \sim 100$ keV, polarization is two times smaller than that given in the Thomson scattering approximation.

Variation of the optical depth also strongly affects the angular distribution of radiation and the polarization degree. An increase in τ_0 leads to more beaming along the normal to the slab and to smaller P (Sunyaev & Titarchuk 1985). At larger $\tau_0 \sim 3$ and $n \gg 1$ (see $n = 10$ curve at the lower panel in Fig. 2) the polarization changes the sign for some angles reminding the behavior of P for $\tau_0 = 1$ and $n = 3$.

Since in the process of thermal Comptonization the energy of a photon increases with the number of scattering, there is one-to-one correspondence between scattering order and the energy. For our further calculations we choose optical depth $\tau_0 = 1$ since the X-ray spectra of accreting neutron stars at low and intermediate luminosities are often described by thermal Comptonization in a slab of optical depth of order unity and electron temperature $kT_e \sim 50$ keV (Gilfanov et al. 1998; Barret et al. 2000; PG03). Polarization degree for larger and smaller τ_0 can be estimated from Fig. 2.

3.2. X-ray bursts

If during the X-ray bursts, we can observe coherent pulsations, the atmosphere is pinned down to the neutron star surface, and thus a plane-parallel approximation is still valid. In a classical problem of radiative transfer in a plane-parallel semi-infinite ($\tau_0 \rightarrow \infty$) atmosphere with opacity dominated by Thomson scattering (Chandrasekhar & Breen 1947; Chandrasekhar 1960; Sobolev 1949; Sobolev 1963), the intensity of escaping radiation is approximated by the formula $I(\mu) \sim 1 + 2.06\mu$. The degree of polarization is at its maximum, 11.7%, at $\mu = 0$ and decreases to 0% at $\mu = 1$ due to the symmetry. The polarization degree can be approximated as

$$P = -\frac{1 - \mu}{1 + 3.582\mu} 11.71\%. \quad (41)$$

The dominant direction of the electric vector oscillations is perpendicular to the meridional plane.

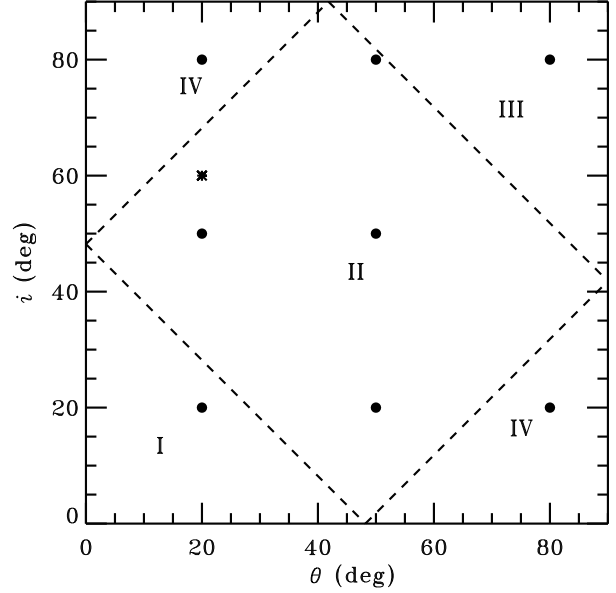


Fig. 3. Classes of the light curves for two antipodal spots and $R = 2.5r_g$ according to Beloborodov (2002). Asterisk shows our basic parameter set and circles correspond to other considered cases.

4. Results

4.1. Pulse profiles for black body spots

The light curves produced by two small antipodal spots emitting as a black body can be divided into four classes (B02, see Fig. 3): I – only one spot is visible, II – the primary spot is always visible, the secondary spot is visible sometimes, III – both spots are eclipsed sometimes, IV – both spots are visible all the time. The light curve from a single spot in Beloborodov’s approximation can be represented as follows (PG03; Poutanen & Beloborodov, in preparation):

$$\begin{aligned} F &\propto \delta^5 [r_g/R + (1 - r_g/R) \cos \psi] \\ &\approx \left(1 - 5\beta \sqrt{1 - r_g/R} \sin i \sin \phi\right) (Q + U \cos \phi), \end{aligned} \quad (42)$$

where

$$\begin{aligned} U &= (1 - r_g/R) \sin i \sin \theta, \\ Q &= r_g/R + (1 - r_g/R) \cos i \cos \theta. \end{aligned} \quad (43)$$

Here we took into account only the first term of the expansion of the Doppler factor in velocity β and approximated $\sin \alpha / \sin \psi$ by its asymptotic value for small angles $\sqrt{1 - r_g/R}$. Thus for small β , the observed flux varies as a sinusoid. At high rotational frequencies, the oscillations are shifted in phase and a harmonic appears as a result of Doppler effect. An additional source of the phase shift and the signal at the harmonic is the light travel delays (see Eq. (13)). One can notice that the exchange of i and θ does not affect the light curve (for small β) since the flux depends on the combinations $\sin i \sin \theta$ and $\cos i \cos \theta$ (see Eqs. (5), (13), (42), (43)).

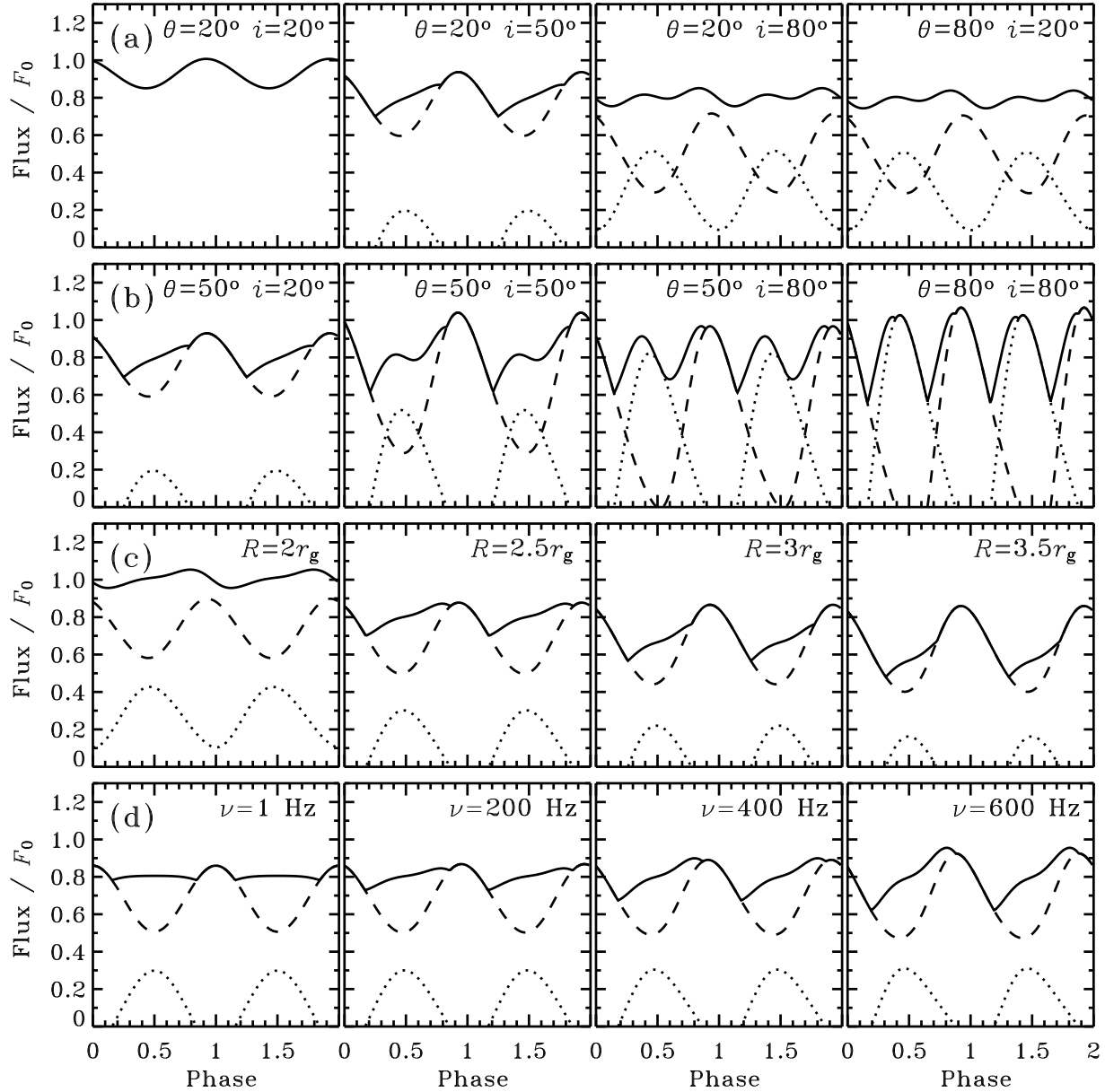


Fig. 4. Observed flux from two antipodal black body spots as a function of phase $\phi_{\text{obs}}/(2\pi)$. The basic set of parameters is $\theta = 20^\circ$, $i = 60^\circ$, $\nu = 300$ Hz, $R = 2.5r_g$ and $M = 1.4M_\odot$. **a), b)** Dependence on the inclination angle i and the magnetic angle θ with other parameters from the basic set. Dependence on the neutron star compactness is shown in panels **(c)**, while panels **(d)** show the effect of different spin frequency. Solid curves correspond to the total flux, while the dashed curves are for the primary spot, and dotted curves – for the secondary.

In Fig. 4a,b we plot the light curves for different couples of i, θ shown in Fig. 3. The phase shift due to the light travel effect is computed relative to the photons emitted at $\phi = 0$ (so that the observed phase 0 coincides with the pulsar phase $\phi = 0$). For a given θ , the variability amplitude from a single spot is increasing with i since polar angle α covers a larger interval. The semi-amplitude is simply

$$A \equiv (F_{\text{max}} - F_{\text{min}})/(F_{\text{max}} + F_{\text{min}}) \approx U/Q. \quad (44)$$

The three panels on the top row show the effect of varying inclination only. At small inclinations, only primary spot is visible (class I) and deviations from the sine wave are small.

At larger inclination, the second spot appears at some moments (class II), when the flux from the first spot is at minimum. The total variability amplitude then decreases. For a slowly rotating star, the increase in the second spot flux would exactly cancel the decrease of the flux from the first spot making a plateau in the total flux. This does not happen when the star rotates at 300 Hz. Rapid rotation introduces an asymmetry, boosting the radiation when the spot is moving towards the observer. Since the peak of the Doppler factor reaches the maximum quarter of the period earlier than the projected area, the peak of the light curve shifts to an earlier phase. At very large inclinations (third panel a), both spots are visible all the time. The light curve be-

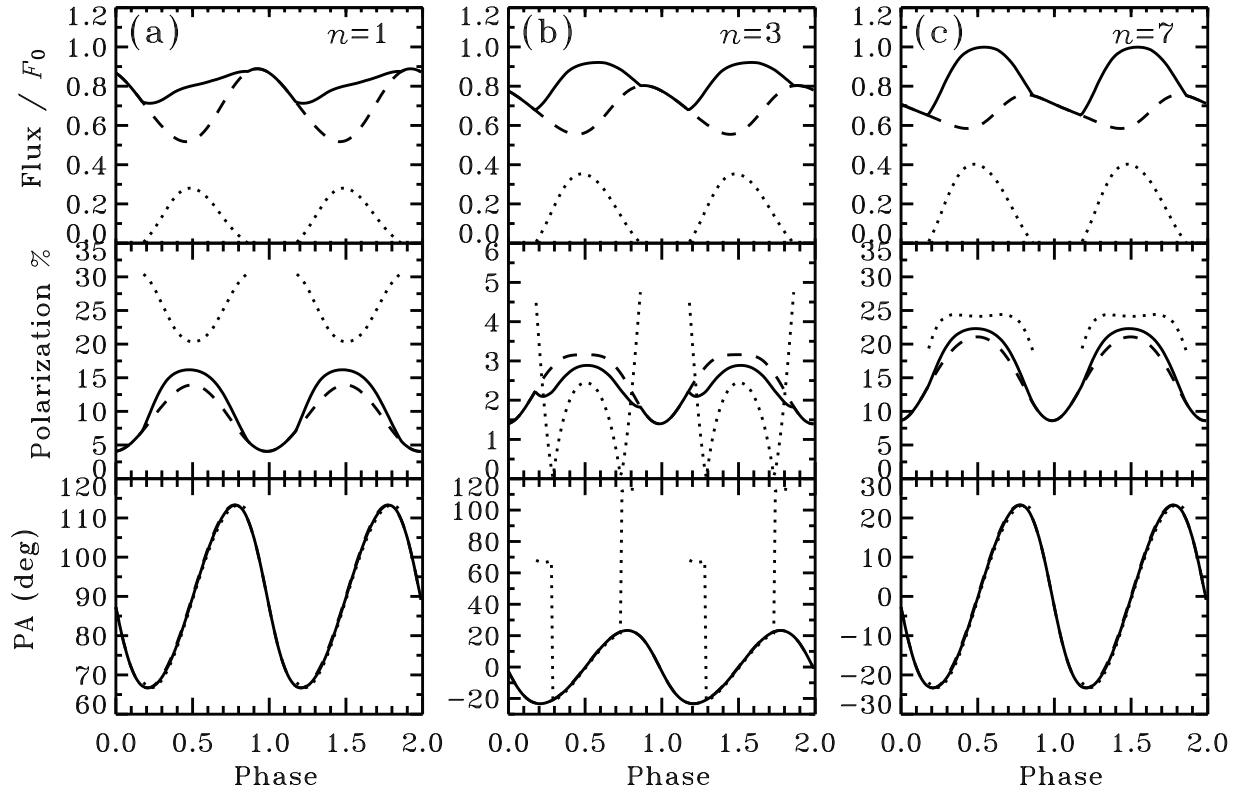


Fig. 5. Pulse profiles of the flux, polarization degree, and polarization angle of the scattered radiation for different scattering orders. The emission region is a slab of Thomson optical depth $\tau_0 = 1$. The same basic set of parameters and the same designations for the curves are used as in Fig. 4.

longs to the class IV and in the absence of rotation would be flat (B02). The variability amplitudes at the fundamental frequency and its harmonic, proportional to $\propto \nu \sin 2i \sin 2\theta$ and to $\propto \nu \sin^2 i \sin^2 \theta$, respectively (Poutanen & Beloborodov, in preparation), are small.

The light curves for other values of inclination i and the magnetic angle θ are shown in Fig. 4b. One sees that exchange i and θ has no effect on the light curve as was noticed above on theoretical grounds (see Eqs. (42), (43)). The variability amplitude for individual spots increases with θ since it is approximately proportional to $\sin \theta$ as can be seen from Eq. (44). At very large i and θ (rightmost panel Fig. 4b), both spots are sometimes eclipsed. Two plateaus, that would appear for slowly rotating stars when both spots are visible, are not present when rotation is fast. Two pulses corresponding to the two spots are almost identical producing a strong signal at a harmonic frequency.

Figure 4c demonstrates the dependence of the light curves on the neutron star compactness M/R . For large compactness, i.e. small radius $R \lesssim 2r_g$, both spots are always visible (class IV) for most of the parameters i, θ . The variability amplitude is a linear function of the spot velocity. For larger radii, the second spot becomes eclipsed (for the set of parameters chosen), and the variability amplitudes grows. This can be easily understood from Eq. (44).

The dependence on the rotational frequency is shown in Fig. 4d. For very slow rotation speed the individual profiles are close to pure sinusoids and the total profile is symmetric with flat parts at the phases where both spots are visible (B02). The larger is the spin frequency, the more the individual profiles become skewed and the more distorted is the total profile. The individual pulse amplitudes also slightly increase with increasing frequency due to variations in the Doppler factor.

4.2. Pulse profiles and polarization of the Comptonized emission

The spectra of accreting millisecond pulsars can be represented as a sum of a black body-like emission and a Comptonized tail (Gilfanov et al. 1998; Gierliński et al. 2002; PG03; Markwardt et al. 2002; Galloway et al. 2002). The black body photons play also a role of seed photons for Comptonization. Since below a few keV contribution of the black body is large the expected polarization degree is small (unless this emission is a Wien peak from electron-scattering dominating atmosphere which can be polarized). Scattering in the hot electron slab modifies significantly the angular distribution of radiation and produces polarization signal as described in § 3 (see also Poutanen & Svensson 1996). The polarization degree is a strong function of the scattering order for small n (see Fig. 2) and therefore the energy (close to the peak of the black body). After 7–10

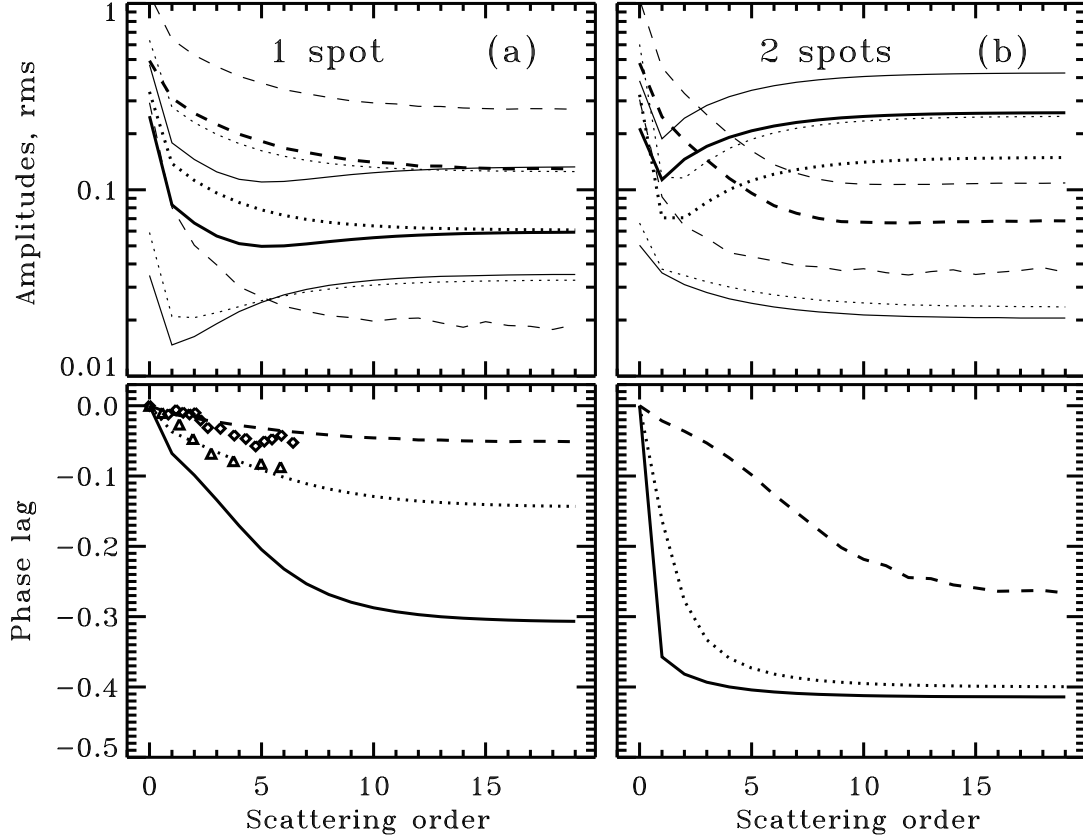


Fig. 6. The amplitudes of the fundamental $a_1(n)$ and the first harmonic $a_2(n)$ (thin curves, fundamental has a larger amplitude) and the total rms (thick curves) as a function of the scattering order are shown in the top panels. Solid, dotted, and dashed curves correspond to the slab optical depth $\tau_0 = 0.5, 1, 3$, respectively. The model phase lags at the fundamental frequency relative to $n = 0$, $\phi_1(n) - \phi_1(0)$ (thick curves), and those at the first harmonic, $\phi_2(n) - \phi_2(0)$ (thin curves), are shown in the lower panels. Left panels (a) correspond to one spot and right panels (b) to two antipodal spots. The parameters are: $i = 60^\circ$, $\theta = 20^\circ$, $R = 2.5r_g$, $M = 1.4M_\odot$. The pulsar frequency was chosen $\nu = 401$ Hz which corresponds to that of SAX J1808.4–3658. The observed phase lags from that source are shown in lower panel (a) by triangles. We transformed the photon energy to the scattering order using Eq. (17) with $kT_e = 50$ keV and $E_0 = 2.8$ keV. Diamonds represent the phase lags observed in the 2.3 ms (435 Hz) accreting pulsar XTE J1751–305 (Gierliński & Poutanen, in preparation).

scatterings polarization saturates. For most of the simulations below we use $n = 7$. This would correspond to about 10 keV for a typical electron temperature of 50 keV and the seed photon temperature of 0.6 keV. At higher T_e , the corresponding energy is higher, while polarization at 10 keV is then smaller. Increase of the electron temperature generally have a depolarizing effect (Poutanen 1994). We choose the slab optical depth $\tau_0 = 1$ which is consistent with the spectra of SAX J1808.4–3658 (PG03). The predicted polarization degree anti-correlates with the value of τ_0 (a smaller τ_0 would increase it and vice versa).

Since the polarized flux corresponds to a power-law like Comptonized spectrum, we use Eq. (21) for the calculations. The polarization degree for individual spots is determined by the polar angle α' in the spot comoving frame and we plot its absolute value. The total polarization degree is given by Eq. (33). The polarization angle is given by Eqs. (25)–(30). If the polarization degree $P(\alpha')$ is negative (in our convention this corresponds to the electric vector oscillations perpendicular to

the meridional plane formed by a photon momentum and a local normal to the slab), we rotate the PA for individual spots by 90° . The total polarization angle is defined by Eq. (34).

First, in Fig. 5 we show the dependence of the flux and polarization profiles on the scattering order. Radiation scattered once is beamed along the normal to the slab similar to a black body radiation ($I(\mu) \approx \text{const}$). The flux profiles are thus almost identical to those for the black body spots (compare left panel in Fig. 5 to the 2nd panel of Fig. 4c) with the maximum close to the zero phase. The polarization degree is always negative at first two scattering orders as can be seen from Fig. 2. The PA is then varies around 90° . The polarization degree is larger for the secondary spot because we see it at grazing angles. However, the observed flux is larger for the primary spot and hence the total degree of polarization is determined by the primary. For each spot, the polarization is larger when the flux is lower because polarization is a monotonic function of $\mu = \cos \alpha'$ which also controls the flux.

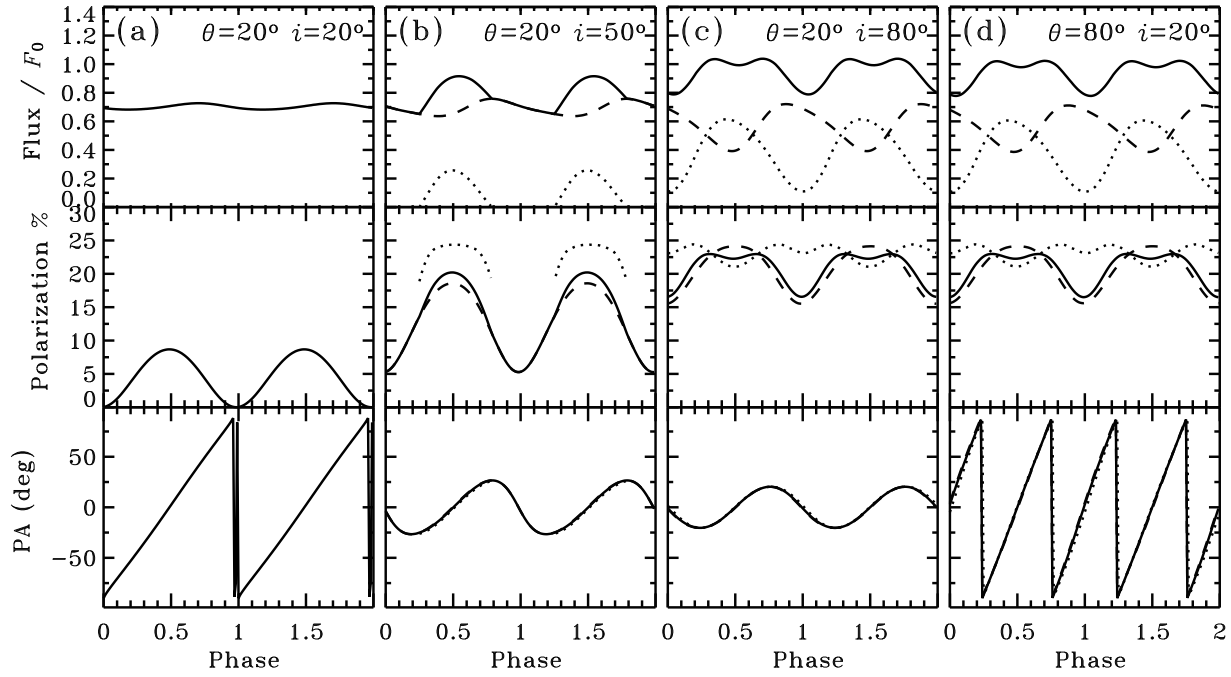


Fig. 7. Same as Fig. 5, but for scattering order $n = 7$ and varying inclination i and magnetic angle θ .

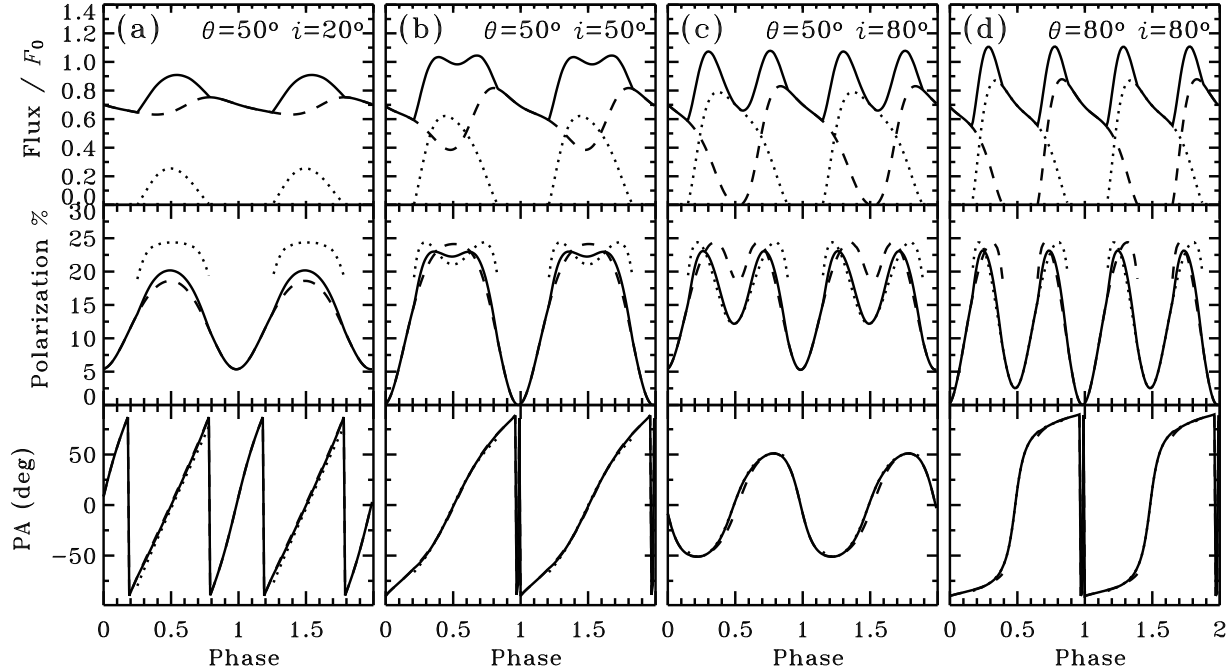


Fig. 8. Same as Fig. 7, for another set of parameters θ and i .

With increasing n the escaping flux becomes less dependent on the polar angle resulting in the reduction of the variability for a primary spot. The intensity at large angles from the normal increases causing a relative increase of the flux from the secondary spot (which is visible at large angles). The total flux is now peaked at phase 0.5 when the secondary has the max-

imum. At the third scattering, the polarization degree defined by Eq. (39) changes sign for smaller polar angles, being still negative for larger ones. The PA for the primary spot (which is observed closer to face-on) now varies around 0° , while the secondary spots, observed at grazing angles, demonstrates a jump in the PA when polarization changes the sign. For scattering

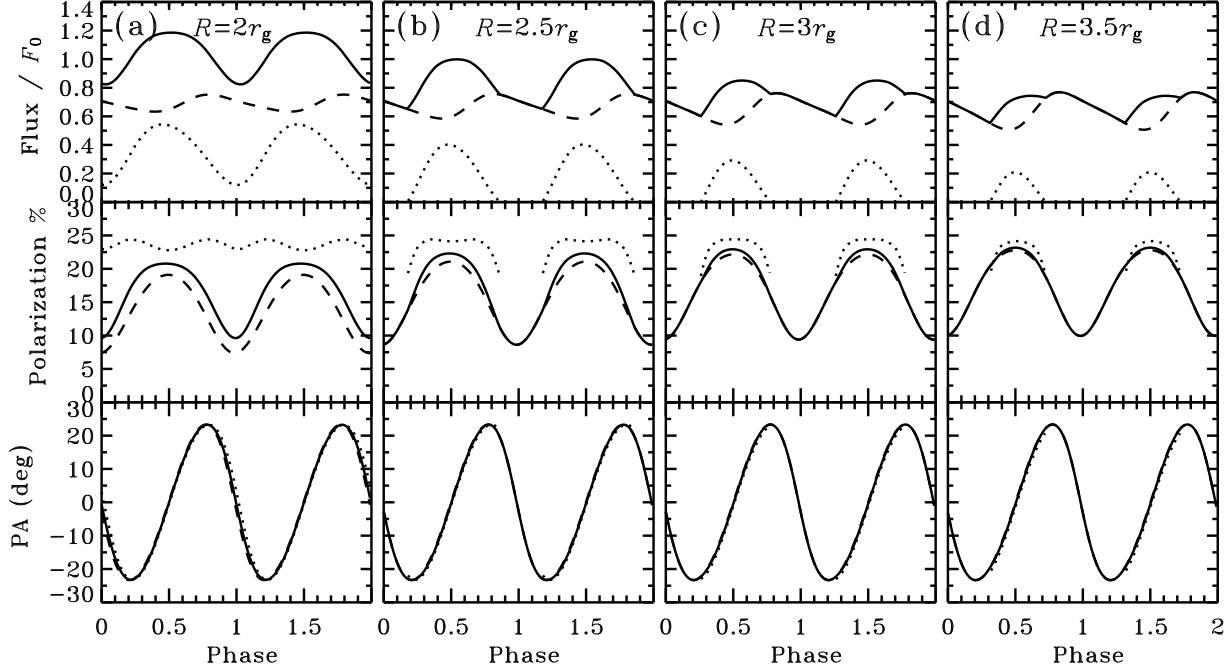


Fig. 9. Same as Fig. 7, but for varying neutron star compactnesses R/r_g .

order $n = 7$ the polarization degree defined by Eq. (39) is always positive, and thus, the PA for both spots varies around zero degrees. The polarization degree is now not a monotonic function of μ , but reaches a maximum at $\mu \sim 0.2$ ($\alpha' \sim 80^\circ$). One sees that for the secondary spot P does not have the maximum when the flux is minimal since we see the spot at grazing angles (see Fig. 2). The hardly visible deviations in PA of the individual spots are due to a combined effect of the time delay and a different relativistic correction angle given by Eq. (29).

Let us represent the light curve for a given scattering order n as a Fourier series

$$F_n(\phi) = \overline{F}_n \left\{ 1 + \sum_{j=1} a_j(n) \cos[2\pi j(\phi - \phi_j(n))] \right\}, \quad (45)$$

where \overline{F}_n is the mean flux. For a pure sine wave, the rms is $a_1/\sqrt{2}$. The dependences of the rms and the variability amplitudes a_1, a_2 on the scattering order n are shown in Fig. 6 for three optical depths τ_0 . The amplitude of the fundamental is generally a decreasing function of n for one spot (Fig. 6a). If two antipodal spots are present (Fig. 6b), the rms has a minimum at $n = 1 - 2$ when $\tau_0 = 0.5 - 1$. At $n = 0$, the black body is peaked as $I(\mu) = e^{-\tau_0/\mu}$ along the normal to the slab producing large variability. Radiation scattered once has now a radiation pattern which actually is close to a pure black body not covered by a hot slab (see Fig. 2 middle panel). This is known to reduce the variability (B02, see Fig. 5a). At larger n , radiation becomes beamed along the slab surface, secondary spot becomes stronger and variability increases (Fig. 5c).

The phase lags $\phi_j(n) - \phi_j(0)$ relative to unscattered radiation, i.e. $n = 0$, at the fundamental frequency are shown in lower panels of Fig. 6. The negative lags mean that the harder

photons are leading the softer ones. With increasing scattering order the pulse profile shifts to an earlier phase. For one spot (left panel), the phase lag results from a combination of Doppler boosting and a change in the emission pattern. The phase lag is then a smooth function of n . It saturates after 5–10 scattering, when the distribution of photons over the slab does not change anymore. The lags are larger for smaller τ_0 when radiation is stronger beamed along the slab (fan-like emission pattern, see top panel in Fig. 2).

For two spots (right panel), there is a jump by almost half-a-period in the lag dependence at small n and τ_0 . This is again a result of dramatic change in the radiation pattern at small n . At $n = 0$, the light curve is dominated by the primary spot and the peak is close to $\phi = 0$, while at larger n , the peak is reached at phases where the secondary spot is visible. For $\tau_0 = 3$, the radiation pattern changes gradually with n and the phase lags also show a gradual evolution.

Figures 7–8 represent the light curves and polarization profiles for $n = 7$ and different couples of i and θ shown in Fig. 3. We can see the dependence on the inclination at the first three panels of both figures. When i and θ are small, we see only one spot (class I) and the variability amplitude $\propto \sin i \sin \theta$ is also very small. Actually, it is much smaller than that for the black body spot since the flux escaping from the slab after a number of scatterings is more isotropic. The polarization degree is small since we look at the spot almost along the normal. If $i = \theta$, then according to Eq. (25), the PA can be presented as $\tan \chi \approx -1/[\cos i \tan(\phi/2)]$. For small i , this reduces to a linear relation $\chi \approx \phi/2 - \pi/2$ clearly visible in Fig. 7a, while for larger i the $\chi - \phi$ relation is more complicated (see Fig. 8b,d). For small β , the PA crosses the zero at phase $\phi \approx -2\beta/(\sqrt{1 - r_g/R} \sin i)$.

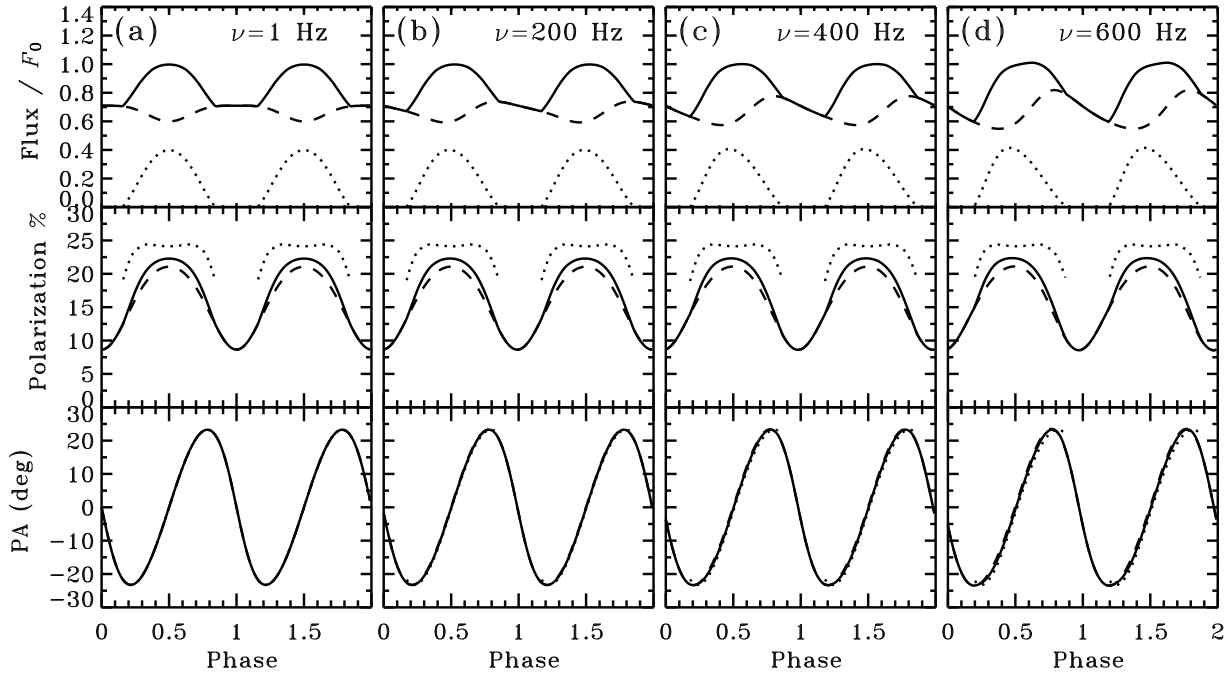


Fig. 10. Same as Fig. 7, but for varying spin frequencies ν .

With increasing inclination, the second spot becomes visible and the oscillation amplitude grows. In class IV, it is actually larger than that for black body spots (compare Fig. 7c to the 3rd panel in Fig. 4a) since the variations of the flux from the two spots do not exactly cancel each other. The polarization also grows with i since we see the spots at larger angles. In Fig. 7b we also see that polarization from the primary spot anti-correlates with corresponding flux, while for the secondary spot they are correlated. This is related to the fact that the primary spot is observed at small polar angles $\mu \sim 1$ where flux and polarization (see Fig. 2) are anti-correlated, while the secondary spot is observed at larger angles where the relation reverses. At larger inclinations (see Figs. 7c, 8b,c) the relation between the polarization (from the secondary) and the flux is not monotonic since we observe the spot at intermediate angles. The PA varies around zero and is close to a sinusoid $\chi \approx -(\tan \theta / \sin i) \sin \phi$ at large inclination and small θ (see Figs. 7b,c, 8c). When both i and θ are large (e.g. Fig. 8d), the flux and polarization degree vary mostly at the harmonic of the spin frequency since the visibility conditions for both spots are similar. The PA, however, varies with the spin frequency.

As we pointed out in § 4.1, the flux profile is (almost) invariant to exchanging i and θ . The degree of polarization is also invariant. The PA, on the other hand, shows completely different behavior: when $i > \theta$ the variations are small, but in the opposite case PA makes a full turn of 360° (compare Fig. 7b to Fig. 8a and Fig. 7c to Fig. 7d). At $i < \theta$, the PA is almost a linear function of the phase, with the derivatives

$$\left. \frac{d\chi}{d\phi} \right|_{\phi=0} = \frac{\sin \theta}{\sin(\theta - i)}, \quad \left. \frac{d\chi}{d\phi} \right|_{\phi=\pi} = \frac{\sin \theta}{\sin(\theta + i)}. \quad (46)$$

The compactness of the neutron star influences the gravitational bending and changes the angle the spots are observed at. For small radius, bending is strong and both spots can be visible all the time (class IV light curve, see Fig. 9a), while at larger radius the light curve class can change to II or even I (Fig. 9b-d). The polarization degree slightly increases with R (effect is clearly visible for the primary spot), since for the given angle ψ , $\cos \alpha \approx r_g/R + (1 - r_g/R) \cos \psi$ is a monotonically decreasing function of R . The effect of the radius on the PA is tiny since only (small) correction angle (29) depends on it.

The influence of the neutron star spin is shown in Fig. 10. Increasing ν modifies mostly the flux profile, since it is proportional to the Doppler factor in power $\Gamma + 3$. The peak shifts towards the phase where the Doppler factor reaches the maximum (a quarter of the period before the peak of the projected area). The pulse profiles thus become more skewed. The polarization degree depends on $\cos \alpha' = \delta \cos \alpha$, which varies only slightly with the spin. The PA is affected through the correction angle which is a linear function of ν (see Eq. (29)) and is small. The time delay slightly shifts all the profiles, especially those for the secondary spot.

4.3. Phase lags in accreting millisecond pulsars

The detailed fitting of the light curves predicted by our models to the data is outside the scope of this paper (see e.g. PG03 for applications to SAX J1808.4–3658). We just compare here the general evolution of the pulse profile with energy which is quantified by the phase lags. We show the phase lags observed from the first accreting ms pulsar SAX J1808.4–3658 (Cui et al. 1998; Gierliński et al. 2002) in the lower panel of Fig. 6a. One sees that the observed behavior is consistent with

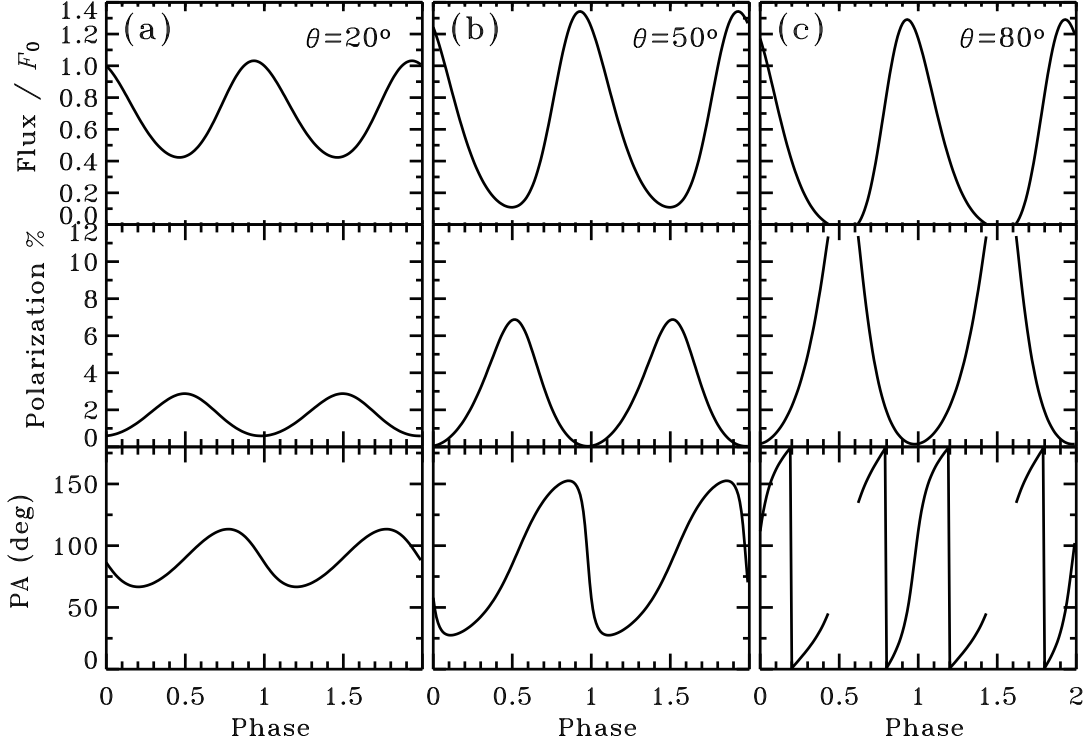


Fig. 11. Light curves, polarization degree and polarization angle expected from an X-ray burst. Semi-infinite electron scattering atmosphere is considered. The parameters are $M = 1.4M_{\odot}$, $i = 60^{\circ}$, $R = 2.5r_g$, $\nu = 400$ Hz.

the model predictions for a single spot and optical depth of the slab of $\tau_0 = 1$. Such an optical depth is in turn consistent with the observed X-ray spectra from the source (PG03). SAX J1808.4–3658 shows almost sinusoidal variations which cannot be described by two-spot model. As is shown in PG03, most probably, the second antipodal spot is blocked from the observer by the accretion disk which inner radius has to be smaller than a few neutron star radii.

The second accreting ms pulsar XTE J1751–305 has pulse profiles which are almost identical to those of SAX J1808.4–3658 with somewhat smaller rms amplitude (Markwardt et al. 2002). Again, only one spot seems to be visible. The spectral analysis (Gierliński & Poutanen, in preparation) shows that the optical depth of the Comptonizing medium is $\tau_0 \sim 2$. According to the model, the phase lags then are smaller than those for $\tau_0 \sim 1$. Observations confirm (diamonds at the lower panel Fig. 6a) that this indeed is the case. One should note here that XTE J1751–305 has a slightly different pulsar period (2.3 ms vs 2.5 ms in SAX J1808.4–3658), therefore the model predictions should be changed accordingly.

We emphasize that the model phase lags are computed relative to the zeroth scattering order (black body), while the observed lags are computed relative to the ~ 3 keV energy band where photons scattered in the hot slab can provide significant contribution. It is encouraging that this simplified model provides a good description of the data. At this stage, however, a detailed comparison seems unjustified.

4.4. X-ray bursts

The X-ray bursts often show coherent oscillations (see Strohmayer & Bildsten 2003). The energy dissipation takes place deep in the electron scattering atmosphere, and thus we can assume that Thomson optical depth is infinite. The escaping intensity in that case is $I(\mu) \propto 1 + 2\mu$ and polarization is 11.7% at maximum when the spot is viewed edge-on (see dashed curves in Fig. 2). The predicted pulse profiles and behavior of polarization degree and angle are shown in Fig. 11. Since the radiation pattern is peaked sharper along the normal than that of the black body, the variability amplitude is larger (compare Fig. 11a to 2nd panels in Fig. 4a,b). The polarization is increasing with the spot colatitude θ reaching the maximum of $\sim 12\%$ close to the eclipses. The PA varies around 90° as the electric vector is predominantly perpendicular to the meridional plane and the amplitude grows with θ .

5. Summary

In this work we have developed a formalism to compute waveforms and polarization profiles from accreting millisecond pulsars and coherent oscillations in X-ray bursts. The radiation from emission region was assumed to be produced as a result of Compton scattering in the accretion shock of Thomson optical thickness ~ 1 (in the case of accretion-powered sources) or optically thick electron atmosphere (in the case of X-ray bursts). The observed flux and polarization are affected by special and general relativistic effects, such as Doppler boosting,

relativistic rotation of the polarization plane, light bending, and gravitational redshift. The developed technique is accurate and extremely efficient from the computational point of view.

Future polarimetric observations in the X-ray domain will serve as a powerful tool in determining the geometry of the emission region in rapidly rotating neutron stars showing coherent millisecond oscillations. Our simulations are the first step in theoretical modelling of these sources.

Acknowledgements. This work was supported by the Academy of Finland, the Jenny and Antti Wihuri Foundation, and the NORDITA Nordic project on High Energy Astrophysics.

References

- Barret, D., Olive, J. F., Boirin, L., et al. 2000, *ApJ*, 533, 329
- Basko, M. M., & Sunyaev, R. A. 1976, *MNRAS*, 175, 395
- Bellazzini, R., Angelini, F., Baldini, L., et al. 2003, in *Proc. of the SPIE 4843, Polarimetry in Astronomy*, ed. S. Fineschi, 383
- Beloborodov, A. M. 2002, *ApJ*, 566, L85 (B02)
- Blaskiewicz, M., Cordes, J. M., & Wasserman, I. 1991, *ApJ*, 370, 643
- Braje, T. M., Romani, R. W., & Rauch, K. P. 2000, *ApJ*, 531, 447
- Bulik, T., Gondek-Rosinska, D., Santangelo, A., et al. 2003, 404, 1023
- Chandrasekhar, S., & Breen, F. H. 1947, *ApJ*, 105, 435
- Chandrasekhar, S. 1960, *Radiative Transfer* (New York: Dover)
- Costa, E., Soffitta, P., Bellazzini, R., et al. 2001, *Nature*, 411, 662
- Cui, W., Morgan, E. H., & Titarchuk, L. 1998, *ApJ*, 504, L27
- Drake, J. J., Marshall, H. L., Dreizler, S., et al. 2002, *ApJ*, 572, 996
- Galloway, D. K., Chakrabarty, D., Morgan, E. H., & Remillard, R. A. 2002, *ApJ*, 576, L137
- Gierliński, M., Done, C., & Barret, D. 2002, *MNRAS*, 331, 141
- Gilfanov, M., Revnivtsev, M., Sunyaev, R., & Churazov, E. 1998, *A&A*, 338, L83
- Ferguson, D. C. 1973, *ApJ*, 183, 977
- Ferguson, D. C. 1976, *ApJ*, 205, 247
- Markwardt, C. B., Swank, J. H., Strohmayer, T. E., in 't Zand, J. J. M., & Marshall, F. E. 2002, *ApJ*, 575, L21
- Marshall, H. L., Murray, S. S., Chappell, J. H., et al. 2003, in *Proc. of the SPIE 4843, Polarimetry in Astronomy*, ed. S. Fineschi, 360
- Miller, M. C., Lamb, F. K., & Psaltis, D. 1998, *ApJ*, 508, 791
- Misner, C. W., Thorne, K. S., & Wheeler, J. A. 1973, *Gravitation* (San Francisco: Freeman)
- Nagirner, D. I., & Poutanen, J. 1993, *A&A*, 275, 325
- Pechenick, K. R., Ftaclas, C., & Cohen, J. M. 1983, *ApJ*, 274, 846
- Poutanen, J. 1994, *ApJS*, 92, 607
- Poutanen, J., & Gierliński, M. 2003, *MNRAS*, 343, 1301 (PG03)
- Poutanen, J., & Svensson, R. 1996, *ApJ*, 470, 249
- Radhakrishnan, V., & Cooke, D. J. 1969, *Ap. Letters*, 3, 225
- Rybicki, G. B., & Lightman, A. P. 1979, *Radiative Processes in Astrophysics* (New York: Wiley-Interscience)
- Sobolev, V. V. 1949, *Uch. Zap. Leningrad Univ.*, 16
- Sobolev, V. V. 1963, *A Treatise on Radiative Transfer* (Princeton: Van Nostrand)
- Sunyaev, R. A., & Titarchuk, L. G. 1985, *A&A*, 143, 374
- Strohmayer, T. 2001, *Adv. Sp. Res.*, 28, 511
- Strohmayer, T., & Bildsten, L. 2003, in *Compact Stellar X-Ray Sources*, ed. W. H. G. Lewin, M. van der Klis (Cambridge: Cambridge University Press) (astro-ph/0301544)
- Thorsett, S. E., & Chakrabarty, D. 1999, *ApJ*, 512, 288
- Thoma, M. H., Truemper, J., & Burwitz, V. 2004, *J. Phys. G30*, S471
- van der Klis, M. 2000, *ARA&A*, 38, 717
- Weinberg, N., Miller, M. C., & Lamb, D. Q. 2001, *ApJ*, 546, 1098
- Wijnands, R. 2004, in *X-Ray Timing 2003: Rossi and Beyond*, ed. P. Kaaret, F. K. Lamb, & J. H. Swank (Melville, NY: AIP), p. 209